

Solution of the Span-Wagner equation of state using a density-energy state function for fluid-dynamic simulation of carbon dioxide

Knut Erik Teigen Giljarhus,* Svend Tollak Munkejord,* and Geir Skaugen*

SINTEF Energy Research, P.O. Box 4761 Sluppen, NO-7465 Trondheim, Norway

E-mail: Knut.Erik.Giljarhus@sintef.no; Svend.T.Munkejord@sintef.no; Geir.Skaugen@sintef.no

Abstract

With the introduction of carbon capture and storage (CCS) as a means to reduce carbon emissions, a need has arisen for accurate and efficient simulation tools. In this work, we propose a method for dynamic simulations of carbon dioxide using the Span–Wagner reference equation of state. The simulations are based on using the density and internal energy as states, which is a formulation naturally resulting from mass and energy balances. The proposed numerical method uses information about saturation lines to choose between single-phase and two-phase equation systems, and is capable of handling phase transitions. To illustrate the potential of the method, it is applied to simulations of tank depressurization, and to fluid-dynamic simulations of pipe transport.

*To whom correspondence should be addressed

Introduction

Carbon capture and storage (CCS) has been proposed as a strategy to reduce carbon emissions to the atmosphere. An important part of the CCS chain is transportation, either in pipelines or in tanks (on boats, vehicles or trains), from a capture point to a storage site. To ensure efficiency and safety in these operations, it is important to have accurate simulation tools to control the processes, and also to perform risk analysis. For instance, an issue with transportation of the supercritical substance (CO_2 is transported at high pressure, in order to minimize pipeline dimensions) is crack propagation. If a pipeline ruptures, the crack may propagate along the pipe depending on the speed of the crack relative to the speed of the expansion wave inside the pipe.^{1,2} To simulate this process, an accurate model for the flow inside the pipe is needed. Another example is the global trade of CO_2 quotas, which has also been suggested as a means to reduce CO_2 emissions.³ From an economic perspective, it is important to accurately describe the CO_2 properties in order to determine the amount of CO_2 stored and transported.

To perform a dynamic simulation, an appropriate mass balance and energy balance is often required for the system of interest. As an example, consider the depressurization of a rigid tank as illustrated in Figure 1. We can set up the following mass balance and energy balance for the problem:

$$V \frac{d\rho}{dt} = -\dot{m}(T, \rho), \quad (1a)$$

$$\frac{dU}{dt} = \dot{Q}(T) - \dot{m}(T, \rho)h(T, \rho). \quad (1b)$$

Here, V is the total volume of the tank, which is constant since the tank is assumed rigid, ρ is the density, \dot{m} is the mass flow rate, U is the internal energy, \dot{Q} is the heat transfer rate, T is the temperature and h is the specific enthalpy. At each time step of a dynamic simulation, we know ρ and U . In order to update these, we need to find the temperature and enthalpy from an equation of state (EOS). The fact that none of the intensive variables are known makes this problem harder to solve than other formulations. The equilibrium condition represents a maximum in the

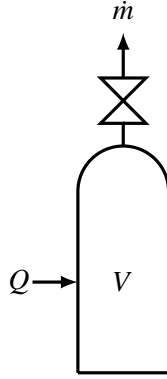


Figure 1: Schematic illustration of a tank.

entropy of the system.⁴ This problem has only been sporadically studied in the literature, and usually for multi-component mixtures. In the context of multi-component mixtures, it is known as the isoenergetic-isochoric flash, or the $UV\mathbf{n}$ flash, where \mathbf{n} is the total number of moles of each component. In this work, however, we work with systems of the type considered in Eq. (1), which translates into a ρu problem, where $u = U/(\rho V)$ is the specific internal energy. The first appearance of the $UV\mathbf{n}$ -formulation known to the authors is Gani et al.,⁵ where it is argued that this formulation has advantages over more traditional approaches. In Flatby et al.,⁶ dynamic simulations of propane-butane mixtures in distillation columns were performed with a $UV\mathbf{n}$ -flash algorithm based on a Newton-Raphson procedure. In Eckert and Kubíček,⁷ a rigorous model for simulating multiple gas-liquid equilibrium stages was developed. This model includes complex multi-phase systems of type gas-liquid-liquid and gas-liquid-liquid-liquid. New phases are dynamically removed and added during the simulation. In Müller and Marquardt,⁸ a faster algorithm for the determination of the number of phases was introduced. In Saha and Carroll,⁹ a partial Newton method was used, along with a novel procedure for generating good initial estimates, to simulate the dynamic filling of a vessel with nitrogen. In Michelsen,⁴ a more sophisticated flash algorithm is devised, which uses stability analysis to determine the number of phases, and a combined solution procedure where a nested-loop procedure is used together with the Newton method to give a robust method with good performance. In Gonçalves et al.,¹⁰ a similar algorithm was used to simulate storage tanks and flash drums. In Castier,¹¹ an optimization algorithm is used to directly maximize the entropy.

This algorithm is used in Castier¹² to simulate vessels with various fluid mixtures. In Arendsen and Versteeg,¹³ the UVn formulation is used to simulate a liquefied gas tank with a propane-butane mixture.

In this work, we are interested in the dynamic simulations involving pure CO_2 . This allows several simplifications to be made compared to a multi-component mixture. Most importantly, the composition is constant (since we only have one component), so saturation curves can be generated a priori and this information can be utilized during simulation. To obtain the thermodynamic properties, we use the Span–Wagner equation of state. In Span and Wagner,¹⁴ an extensive body of experimental data for CO_2 was reviewed, and an EOS fitted to these data was presented. The fitting procedure was based on the thermal properties of the single-phase region, the liquid-vapor saturation curve, the speed of sound, the specific heat capacities, the specific internal energy and the Joule-Thomson coefficient. The equation gives very accurate results, even in the region around the critical point, and is now considered as the most accurate reference equation for CO_2 . It is for instance used in the NIST Chemistry WebBook.¹⁵ There are other alternatives available that are simpler computationally while retaining most of the accuracy, for instance Huang et al.¹⁶ and Kim,¹⁷ and the proposed method can be used with these equations of state as well.

In this work, we present an efficient method for solving the ρu problem for pure CO_2 using the Span–Wagner (SW) EOS. Although the equation is complicated and contains many terms, we demonstrate that it is feasible to use it in dynamic simulations. We compare the speed of the method to an equivalent procedure from the NIST software package REFPROP.¹⁸ We also compare the results to results obtained with simpler equations of state, the stiffened gas (SG) EOS^{19,20} and the Peng–Robinson (PR) cubic EOS.²¹ The presented method can also easily be used with other equations of state, for instance the two alternative equations of state mentioned above,^{16,17} or equations of state for other substances like the reference equation of state for nitrogen from Span et al..²² It can also be applied to multi-component mixtures, if the composition is constant. To demonstrate the utility of the proposed method, we apply the algorithm to the dynamic simulation of

tank filling, and to a fluid-dynamic simulation of pipe transport. In a fluid-dynamic simulation, there can be sharp gradients in the solution due to shock waves and other discontinuities. Additionally, the simulation can potentially be time consuming due to a large number of cells and small time steps. This puts high demands on the accuracy, robustness and efficiency of the methods used.

Thermodynamics

Thermodynamic properties

If an expression for the (specific) Helmholtz free energy, $a(T, \rho)$ is known, along with its derivatives, all other thermodynamic properties can be derived from this expression. Important properties in this work are pressure, specific entropy, specific enthalpy and specific internal energy, which expressed in terms of the Helmholtz function and its derivatives are

$$P(T, \rho) = \rho^2 \left(\frac{\partial a}{\partial \rho} \right)_T, \quad (2)$$

$$s(T, \rho) = - \left(\frac{\partial a}{\partial T} \right)_\rho \quad (3)$$

$$h(T, \rho) = a + \rho \left(\frac{\partial a}{\partial \rho} \right)_T - T \left(\frac{\partial a}{\partial T} \right)_\rho, \quad (4)$$

$$u(T, \rho) = a - T \left(\frac{\partial a}{\partial T} \right)_\rho. \quad (5)$$

It is common to define a non-dimensional Helmholtz function, $\phi = a/(RT)$, and split this function into an ideal-gas part, ϕ^0 , and a residual part, ϕ^r ,

$$\phi(\tau, \delta) = \phi^0(\delta, \tau) + \phi^r(\delta, \tau). \quad (6)$$

This reduced Helmholtz function is expressed in terms of the reduced density, $\delta = \rho/\rho_c$ and the inverse reduced temperature, $\tau = T_c/T$. ρ_c and T_c are the critical density and the critical temperature,

respectively. The critical properties of CO₂ are summarized in Table 1. Expressed in terms of the reduced Helmholtz energy, the pressure, specific entropy, specific enthalpy and specific internal energy are

$$\frac{P(\tau, \delta)}{\rho RT} = 1 + \delta \frac{\partial \phi^r}{\partial \delta}, \quad (7)$$

$$\frac{s(\tau, \delta)}{R} = \tau \frac{\partial \phi}{\partial \tau} - \phi, \quad (8)$$

$$\frac{h(\tau, \delta)}{RT} = 1 + \tau \frac{\partial \phi}{\partial \tau} + \delta \frac{\partial \phi^r}{\partial \delta}, \quad (9)$$

$$\frac{u(\tau, \delta)}{RT} = \tau \frac{\partial \phi}{\partial \tau}. \quad (10)$$

The Span–Wagner equation of state

The Span–Wagner equation of state is expressed in terms of the reduced Helmholtz energy as described above. The expression for the ideal part is

$$\begin{aligned} \phi^0(\tau, \delta) = & \ln(\delta) + a_1^0 + a_2^0 \tau + a_3^0 \ln(\tau) \\ & + \sum_{i=4}^8 a_i^0 \ln[1 - \exp(-\tau \theta_i^0)]. \end{aligned} \quad (11)$$

The expression for the residual part is

$$\begin{aligned} \phi^r(\tau, \delta) = & \sum_{i=1}^7 n_i \delta^{d_i} \tau^{t_i} \\ & + \sum_{i=8}^{34} n_i \delta^{d_i} \tau^{t_i} \exp(-\delta^{c_i}) \\ & + \sum_{i=35}^{39} n_i \delta^{d_i} \tau^{t_i} \exp(-\alpha_i (\delta - \varepsilon_i)^2 - \beta_i (\tau - \gamma_i)^2) \\ & + \sum_{i=40}^{42} n_i \Delta^{b_i} \delta \exp(-C_i (\delta - 1)^2 - D_i (\tau - 1)^2), \end{aligned} \quad (12)$$

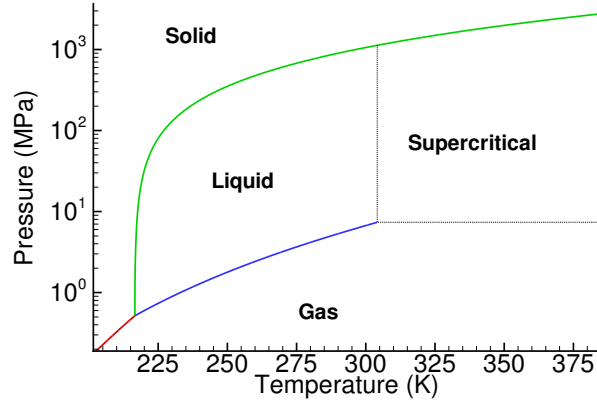


Figure 2: Phase diagram for CO₂.

where $\Delta = \{(1 - \tau) + A_i[(\delta - 1)^2]^{1/(2B_i)}\}^2 + B_i[(\delta - 1)^2]^{a_i}$. The coefficients a_i^0 , θ_0^i , n_i , a_i , b_i , β_i , A_i , B_i , C_i and D_i can be found in the original paper by Span and Wagner,¹⁴ along with expressions for the derivatives of the Helmholtz function.

We see that the equation contains a total of 51 terms, many of which include logarithms and exponentials. This means that this is an expensive function to evaluate, and efficient numerical methods are critical to obtain satisfactory run times for dynamic simulations.

The Span–Wagner equation of state covers the fluid region from the triple-point temperature up to 1100 K and pressures up to 800 MPa. In Span and Wagner,¹⁴ correlations are also given for the vapor pressure, melting pressure and sublimation pressure. Figure 2 shows the phase diagram for CO₂ generated using these correlations.

Table 1: Critical properties of CO₂.

Property	Symbol	Value
Critical density	ρ_c	467.6 kg/m ³
Critical temperature	T_c	304.1282 K
Critical pressure	P_c	7.3773 MPa

Vapor-liquid equilibrium and the ρu algorithm

In an ideally isolated system, all internal processes lead to an increase in the total entropy of the system. When the entropy reaches its maximum value, the system is at equilibrium. In a system with liquid and vapor with no chemical reactions, the equilibrium condition is that the temperature, pressure and the Gibbs free energy must be equal in both phases.

As seen from Eq. (1) for the rigid tank, at each time step of a dynamic simulation, we know the specific internal energy, u^{in} , and the density, ρ^{in} , and want to find the rest of the thermodynamic properties. If the system is single phase, it is sufficient to solve

$$u(T, \rho^{\text{in}}) = u^{\text{in}}, \quad (13)$$

to find the temperature. The rest of the thermodynamic properties can then be found from the Helmholtz free energy. If the system is vapor-liquid, we need to solve

$$\alpha \rho_v u(T, \rho_v) + (1 - \alpha) \rho_l u(T, \rho_l) = \rho^{\text{in}} u^{\text{in}}, \quad (14a)$$

$$\alpha \rho_v + (1 - \alpha) \rho_l = \rho^{\text{in}}, \quad (14b)$$

$$P(T, \rho_v) = P(T, \rho_l), \quad (14c)$$

$$G(T, \rho_v) = G(T, \rho_l), \quad (14d)$$

to find T , ρ_v , ρ_l and α , where $\alpha = V_v/V$ is the vapor volume fraction and G is the Gibbs free energy.

Our algorithm is based on the fact that we can determine whether we have one or two phases based on the values ρ^{in} and u^{in} . Figure 3 shows the phase boundary in the (ρ, u) plane, drawn using the Span–Wagner equation of state. Before the simulation starts, this phase diagram is generated and stored as a polygon, where the inside of the polygon denotes the vapor-liquid region. The phase diagram can be generated by using the Span–Wagner equation of state to find saturation lines using an iterative procedure, see e.g. Michelsen and Mollerup,²³ Chap. 12. During the simulation, it is

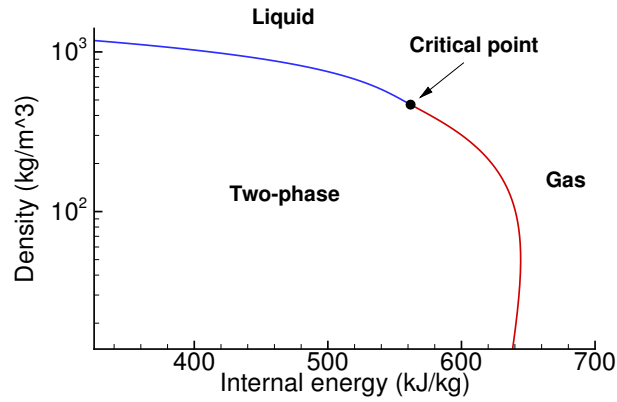


Figure 3: Phase diagram for CO₂ in the (ρ, u) plane.

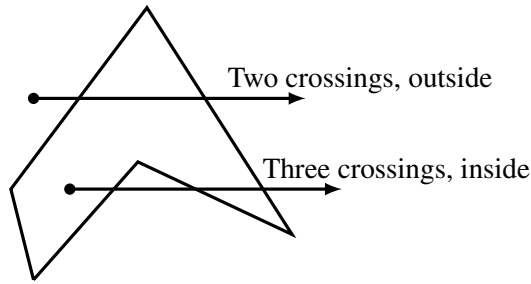


Figure 4: Illustration of the ray-crossing algorithm.

determined if a given point lies within the polygon. If it does, Eq. (14) is solved, and if it is outside, Eq. (13) is solved. Several different strategies for determining whether a point is inside a polygon exist, and a good summary is given in Haines.²⁴ Here, we choose a general algorithm based on ray-crossing. Faster point-in-polygon algorithms exist, for instance by using lookup grids. However, this introduces higher complexity and higher memory use, and as demonstrated later, the point inclusion test only constitutes a small part of the total run time. The ray-crossing algorithm works by shooting a ray from the test point along the x -axis and counting the number of times the ray crosses the polygon boundary. According to the Jordan curve theorem, every time the boundary is crossed, the ray switches between inside and outside. If the number of ray crossings is odd, the point is inside the polygon. See Figure 4 for an illustration. This algorithm has a computational complexity of $O(n)$, where n is the number of points in the polygon. In this work, we use 200 points. Since the (ρ, u) polygon is a convex polygon, a simple optimization is to stop the inclusion test after two crossings have occurred, since by definition a ray shot through a convex polygon can only cross

the boundary two times.

After it has been determined if the point lies in the single-phase or vapor-liquid region, the appropriate equation system must be solved. The actual equations are solved using the Newton-Raphson method. This method can be sensitive to the initial conditions, but since good initial estimates are often available in dynamic simulations, the fast convergence of this method makes it attractive for this application. As initial conditions for the solver, we use values from the previous time step, which are usually close to the actual solution. We evaluate the Jacobian analytically. For the one-phase system, Eq. (13), the Jacobian is

$$\left(\frac{\partial u}{\partial T}\right)_\rho = c_V, \quad (15)$$

where c_V is the specific heat capacity at constant volume. For the two-phase system, Eq. (14), the Jacobian is

$$\begin{bmatrix} \alpha\rho_v c_{V,v} + (1-\alpha)\rho_l c_{V,l} & 0 & P_{T,v} - P_{T,l} & -s_v + \frac{P_{\rho_v}}{\rho_v} + s_l - \frac{P_{\rho_l}}{\rho_l} \\ \alpha u_v + \frac{\alpha}{\rho_v} (P_l - TP_{\rho_l}) & \alpha & P_{\rho_v} & \frac{P_{\rho_v}}{\rho_g} \\ (1-\alpha)u_l + \frac{1-\alpha}{\rho_l} (P_l - TP_{\rho_l}) & 1-\alpha & -P_{\rho_l} & -\frac{P_{\rho_l}}{\rho_l} \\ \rho_v u_v - \rho_l u_l & \rho_v - \rho_l & 0 & 0 \end{bmatrix}. \quad (16)$$

The pressure derivatives are derived in terms of the derivatives of the reduced residual Helmholtz energy as

$$P_T(\delta, \tau) = \rho_c \delta R (1 + \delta \phi_\delta^r(\delta, \tau) - \delta \tau \phi_{\delta\tau}^r(\delta, \tau)), \quad (17)$$

$$P_\rho(\delta, \tau) = \frac{RT_c}{\tau} (1 + 2\delta \phi_\delta^r(\delta, \tau) + \delta^2 \phi_{\delta\delta}^r(\delta, \tau)). \quad (18)$$

If the time step of the dynamical simulation is large, the initial conditions for the Newton iterations may not be good enough to obtain convergence. This is especially the case for the more complex vapor-liquid equilibrium equation system. For this system, the required initial conditions are

T, ρ_l, ρ_g and α . If the Newton-Raphson method fails to converge, it is possible to use estimations for the saturation conditions to get a better guess for the densities. In Span and Wagner,¹⁴ the following simplified correlations for the saturated liquid density and the saturated vapor density are given,

$$\ln\left(\frac{\rho_l}{\rho_c}\right) = \sum_{i=1}^4 a_i \left(1 - \frac{T}{T_c}\right)^{t_i}, \quad (19)$$

$$\ln\left(\frac{\rho_g}{\rho_c}\right) = \sum_{i=1}^5 a_i \left(1 - \frac{T}{T_c}\right)^{t_i}. \quad (20)$$

The constants a_i and t_i are unique for each expression and can be found in the original paper by Span and Wagner.

Fluid dynamics

Governing equations

As an example of the application of the above algorithm, we consider a 1D flow model of two-phase CO₂. For simplicity, we assume that the two phases have equal velocities. The flow can then be described by the Euler equations,

$$\frac{\partial \rho}{\partial t} + \frac{\partial(\rho v)}{\partial x} = 0, \quad (21)$$

$$\frac{\partial(\rho v)}{\partial t} + \frac{\partial(P + \rho v^2)}{\partial x} = 0, \quad (22)$$

$$\frac{\partial(\rho e)}{\partial t} + \frac{\partial[v(\rho e + P)]}{\partial x} = 0. \quad (23)$$

Here, $\rho = \alpha_g \rho_g + \alpha_l \rho_l$ is the mixture density, v is the velocity and $e = u + \frac{1}{2}v^2$ is the total energy. This model is often denoted the *homogeneous* model, and can be accurate if the interphase momentum transfer is high, for instance in highly dispersed flows. An advantage of using this model is that the method to solve the ρu problem also can be applied to multi-component mixtures, since the

composition is constant. Drift-flux models or two-fluid models can also be used without any modifications of the thermodynamic solver, but then only for pure CO₂.

Since this model is meant to illustrate the ρu problem, we ignore other physical effects like pipe friction and gravity. These would typically be included as source terms in the above equation system.

Numerical method

The numerical method we employ is the multi-stage centred approach (MUSTA).^{25,26} This is a finite-volume method which retains much of the simplicity of centred schemes, while approaching the accuracy of more sophisticated upwind schemes. It has also been found to be robust. The method has been employed for various two-phase flow models, including drift-flux models.^{27,28} In the present problem, the complexity lies in the EOS, and the scheme of Titarev and Toro²⁶ can be used rather directly.

The system of Eqs. (21) to (23) can be cast in the following form:

$$\frac{\partial \mathbf{q}}{\partial t} + \frac{\partial \mathbf{f}(\mathbf{q})}{\partial x} = \mathbf{0}, \quad (24)$$

where $\mathbf{q} = [\rho, \rho v, \rho e]^T$ is the vector of conserved variables. Employing the finite-volume method, we obtain the discretized system

$$\mathbf{q}_j^{m+1} = \mathbf{q}_j^m - \frac{\Delta t}{\Delta x} (\mathbf{f}_{j+1/2}^m - \mathbf{f}_{j-1/2}^m), \quad (25)$$

where \mathbf{q}_j^m denotes the numerical approximation to the cell average of the vector of unknowns $\mathbf{q}(x, t_m)$ in control volume j at time step m . In the MUSTA scheme, the numerical flux at the cell interface is

a function of the cell averages on each side:

$$\mathbf{f}_{j+1/2} = \mathbf{f}^{\text{MUSTA}}(\mathbf{q}_j, \mathbf{q}_{j+1}). \quad (26)$$

Further details can be found in Titarev and Toro²⁶ and Munkejord et al.²⁷

The numerical method, Eq. (25), is subject to the Courant–Friedrichs–Lewy (CFL) stability condition. The CFL number is

$$R = \frac{\|\lambda\|_\infty \Delta t}{\Delta x}, \quad (27)$$

where $\|\lambda\|_\infty$ is the maximum eigenvalue of the flux Jacobian matrix of the model (24) in the computational domain. Here we have

$$\|\lambda\|_\infty = \max|v \pm C|, \quad (28)$$

where C is the speed of sound. Note that in the two-phase region, the sound speed of the mixture is the combined result of the thermodynamic relations *and* the flow model. Further, in large parts of the two-phase region, the sound speed of the mixture is smaller than that of pure gas or pure liquid. For the present homogeneous flow model, the mixture speed of sound can be calculated analytically using Eq. (6.15) of Flåtten and Lund,²⁹

$$C_{\text{mix}}^{-2} = \rho_{\text{mix}}(Z_p + Z_{pT} + Z_{pT\mu}), \quad (29)$$

$$Z_p = \frac{\alpha_g}{\rho_g c_g} + \frac{\alpha_l}{\rho_l c_l}, \quad (30)$$

$$Z_{pT} = \frac{c_{p,g} c_{p,l} T}{c_{p,g} + c_{p,l}} \left(\frac{\Gamma_l}{\rho_l c_l} - \frac{\Gamma_g}{\rho_g c_g} \right)^2, \quad (31)$$

$$Z_{pT\mu} = \frac{\rho_{\text{mix}} T}{c_{p,g} + c_{p,l}} \left(\frac{\rho_g - \rho_l}{\rho_g \rho_l (h_g - h_l)} (c_{p,g} + c_{p,l}) + \frac{\Gamma_g c_{p,g}}{\rho_g C_g^2} + \frac{\Gamma_l c_{p,l}}{\rho_l C_l^2} \right)^2, \quad (32)$$

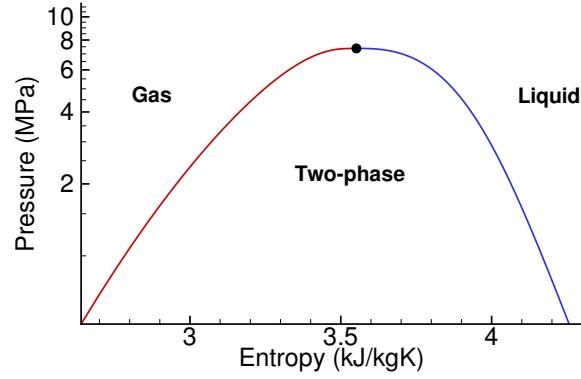


Figure 5: Phase diagram for CO₂ in the (P, s) plane.

where Γ_i is the Grüneisen coefficient,

$$\Gamma_i = \frac{1}{\rho_i} \left(\frac{\partial p}{\partial u_i} \right)_{\rho_i}. \quad (33)$$

Boundary conditions

In a fluid-dynamic simulation, boundary conditions must be specified at the domain boundaries. Here, we implement the boundaries using ghost cells. The *specified-pressure* boundary condition requires extra care. For this boundary condition, we assume an isentropic process, which means that the specific entropy, s , in the ghost cell is taken to be the same value as the first inner cell. The pressure is set to the specified value. The rest of the variables must then be calculated in the ghost cell. The equilibrium value for this Ps problem corresponds to a global minimum in the enthalpy of the system.⁴ However, here we employ the same approach as for the ρu problem. Before the simulation starts, the saturation curve is drawn in the (P, s) plane. This curve is shown in Figure 5. This curve is then used to determine which equation system has to be solved using the

point-in-polygon algorithm. For a single-phase system, the equation system to solve is

$$P(T, \rho) = P^{\text{in}}, \quad (34\text{a})$$

$$s(T, \rho) = s^{\text{in}}, \quad (34\text{b})$$

with T and ρ as unknowns. For a two-phase system, we know that the pressure is the vapor pressure, and we can then determine the temperature and densities directly from the saturation line. It then remains to find the vapor mass fraction, x , which is found by solving

$$xs_g(T, \rho_g) + (1 - x)s_l(T, \rho_l) = s^{\text{in}}. \quad (35)$$

To solve the equations, we use the Newton-Raphson method with numerical derivatives.

Results

This section presents some results from using the proposed algorithm. First, a convergence test is presented to test correctness and efficiency. Then, the algorithm is applied to the tank depressurization problem from the introduction. Finally, some fluid dynamics simulations are presented.

Convergence test

To get an indication of the robustness and performance of the proposed approach, a set of problems was generated by choosing pressures and temperatures, calculating the density and internal energy, and then checking the necessary number of iterations for the algorithm to converge to the initial pressure and temperature. A comparison is also being made to the NIST software package REFPROP,¹⁸ which contains a subroutine DEFLSH that also solves the ρu problem.

Two sets of pressures and temperatures are considered. First, we choose 10000 points in the

single-phase regime, with temperatures ranging from 220 K to 350 K and pressures ranging from 0.1 MPa to 20 MPa. Second, we choose 10000 points along the saturation line with a gas fraction of 0.5 to test convergence in the two-phase regime. In dynamic simulations, the results from the previous time step can often provide a good initial estimate for the non-linear solver. Here, we get the initial condition by perturbing the exact solution by 10%.

The algorithm was able to find the correct solution for all problems, even in the vicinity of the critical region. The total runtime and average number of iterations are given in Table 2. The programs are written in the Fortran programming language, and compiled with the GNU Fortran compiler with the `-O3` optimization flag. The times were taken using the `cpu_time` subroutine on an Intel(R) Core(TM)2 Duo T7700 CPU. The two-phase problems took about 24 times longer to complete. This is because they require more iterations to converge coupled with a more expensive function evaluation. Overall, the total runtime is low considering the number of problems, and is considered adequate for dynamic simulations. The runtime is dominated by the solution of the non-linear system. For the single-phase cases, the point-inclusion test represents about 3% of the total runtime, while for the two-phase cases, only about 0.2% of the time is spent in the point-inclusion test. This justifies the use of the general point-in-polygon algorithm over more sophisticated approaches.

The REFPROP program takes significantly more time to find the solution. For the single-phase case, REFPROP is about 20 times slower, while for the two-phase case, REFPROP is about 16 times slower. Additionally, REFPROP failed to converge for single-phase problems near the melting line.

Table 2: Comparison of total runtime and average number of iterations for solving 10000 $\rho\mu$ -problems in the single-phase and two-phase regimes.

Regime	Total time (s)	Average # of iterations	REFPROP (s)
Single-phase	0.39	2.5	7.54
Two-phase	9.25	5.0	148.35

Tank simulations

In this section, we use the tank model from the introduction, Eq. (1), to simulate the depressurization of a tank. To close the tank model, we need expressions for the heat transfer rate, \dot{Q} , and the mass flow rate, \dot{m} . We model the heat transfer as the heat transfer rate multiplied with the temperature difference between the tank temperature and the ambient temperature, T_{amb} ,

$$\dot{Q}(T) = \eta A (T_{\text{amb}} - T), \quad (36)$$

where η is the overall heat-transfer coefficient and A is the surface area of the tank. The flow rate is modeled using a valve equation,

$$\dot{m} = K_v \sqrt{\rho (P - P_{\text{amb}})}, \quad (37)$$

where K_v is a flow coefficient for the valve and P_{amb} is the ambient pressure. To solve the equations, we use the DASSL differential algebraic equation solver.³⁰

As a test case, we consider a cylindrical tank with diameter 0.2 m and height 1.0 m, with initial state $P_0 = 80$ bar and $T_0 = 25^\circ\text{C}$. The ambient conditions are $P_{\text{amb}} = 6$ bar and $T_{\text{amb}} = 5^\circ\text{C}$. A moderate value of $\eta A = 10$ W/K is used, and the valve coefficient is set to $K_v = 8 \times 10^{-7}$ m². At $t = 0$, the valve is opened to the surroundings. Note that initially, CO₂ is in a compressible liquid state, above the critical pressure, while at steady state it will reach the ambient condition which is in the vapor region. This is a challenging test case, since it covers pure liquid, transition to two-phase and finally transition to pure vapor.

Figure 6 shows the transient development of the contained mass inside the tank, the pressure, the temperature and the vapor volume fraction. There is a fast reduction in temperature and pressure down to the saturation line. The CO₂ then starts to evaporate, and the temperature and pressure continues to decrease until all the liquid has evaporated. When all the liquid has evaporated, the pressure in the vessel has reached about 7.7 bar. Now, heat transfer starts to dominate, and the gas is heated by the ambient and further expanded until the final state of 5°C and 6 bar is reached. In

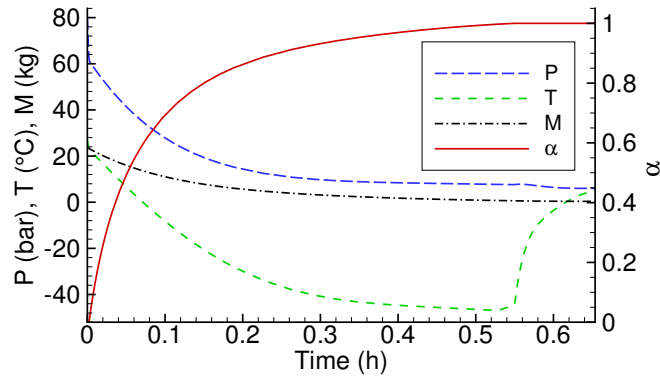


Figure 6: Depressurization of a CO₂ tank. Pressure (P), temperature (T), mass (M) and vapor volume fraction (α) as a function of time.

Figure 7a the same development is shown in a pressure-temperature diagram. The vapor pressure line is indicated as a solid line and the simulation path is shown as a dashed line. The initial point of the simulation is in the liquid region. Saturated conditions are reached after only about 10s at approximately 61 bar and 296K where vapor starts forming due to expansion. At 7.7bar all the (remaining) liquid has evaporated and the vapor is superheated until the ambient temperature is reached. The same process is also shown in the (ρ, u) -plane in Figure 7b. The initial state is just above the saturation line for liquid internal specific energy. Then it expands into, and through, the two-phase region and finally into the vapor region where it is further expanded to reach ambient temperature and pressure. In the first part of the expansion, the internal energy decreases due to the fast initial expansion due to the opening of the valve. After this initial abrupt decrease in pressure, the heat transfer starts to dominate, and the internal energy starts to increase. The density continues to decrease due to the open valve. When all the liquid has evaporated, the vapor is superheated and expanded until the ambient temperature and pressure is reached. The expansion is faster in the pure vapor phase due to the higher compressibility of the vapor.

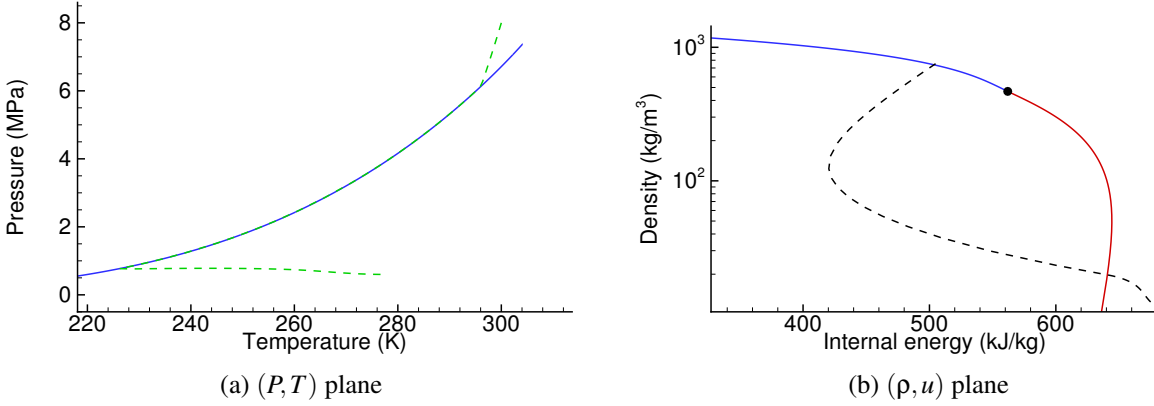


Figure 7: Depressurization of a CO_2 tank. Simulation paths (dashed lines) through the (P, T) and (ρ, u) planes.

Fluid-dynamic simulations

In this section, we present some fluid-dynamic simulations. All test cases are performed in a 100 m long tube/pipe, with 1000 grid cells and a CFL number of 0.9.

Single-phase shock tube

Here, we consider a shock tube where a tube is divided by a membrane with different properties in the two sections. At $t = 0$, the membrane is removed.

For comparison purposes, we have also included results from the stiffened-gas EOS.^{19,20} The SG EOS is attractive because it retains an explicit expression for the pressure as a function of density and internal energy,

$$P(\rho, u) = \rho u(\gamma - 1) - \gamma P_\infty, \quad (38)$$

where P_∞ is a constant. The stiffened-gas equation can be viewed as a linearization about a reference state. By carefully choosing the reference state, and as long as the simulation does not deviate too far from this reference state, good results can be obtained for certain properties. Here, we choose the sound speed, C_0 , as an input parameter to get a good fit for the pressure waves in the shock tube. The other input parameters are the pressure, temperature, density and specific heat capacity at

constant pressure. The rest of the parameters in Eq. (38) are then found from

$$\gamma = \frac{C_0^2}{c_{P,0}T_0} + 1, \quad (39)$$

$$c_V = \frac{c_{P,0}}{\gamma}, \quad (40)$$

$$P_\infty = \rho_0 c_V T_0 (\gamma - 1) - P_0. \quad (41)$$

As a reference state, we use the arithmetic mean of the two tube sections.

Here, we look at a case in the gas phase. The left section is at $P = 3$ MPa and the right section is at $P = 1$ MPa, with a uniform temperature of $T = 300$ K. The results at $t = 0.08$ s are plotted in Figure 8. Due to the pressure difference, the gas starts flowing towards the right. A shock wave also propagates to the right, while a rarefaction wave propagates to the left. We also observe a contact discontinuity in the density and temperature. Our ρu solver is clearly capable of finding the solution even in the presence of sharp gradients. Typically, 2–4 iterations are required in the non-linear solver. We also observe good agreement with the stiffened-gas equation for the pressure waves. For the temperature and density, however, the agreement is not as good, which is due to the inability of the stiffened-gas equation to fully capture the thermodynamic behavior of CO_2 .

The numerical method should converge as the grid size is increased, and no oscillations should be introduced. A demonstration of convergence with grid refinement is shown in Figure 9.

Transition from one-phase to two-phase

Transport of CO_2 in a gaseous state is inefficient because of the low density which gives a relatively high pressure drop per unit length of the pipe. Hence, the transport of CO_2 is typically done in a dense liquid-like state, since this is the most energy efficient condition.³¹ The pressure should also be higher than the critical pressure, to avoid the possibility of evaporation if temperature changes occur along the pipeline. However, during events such as startup and shutdown, or due to critical events such as pipe rupture, the pressure can quickly drop causing transition to two-phase. Here, we

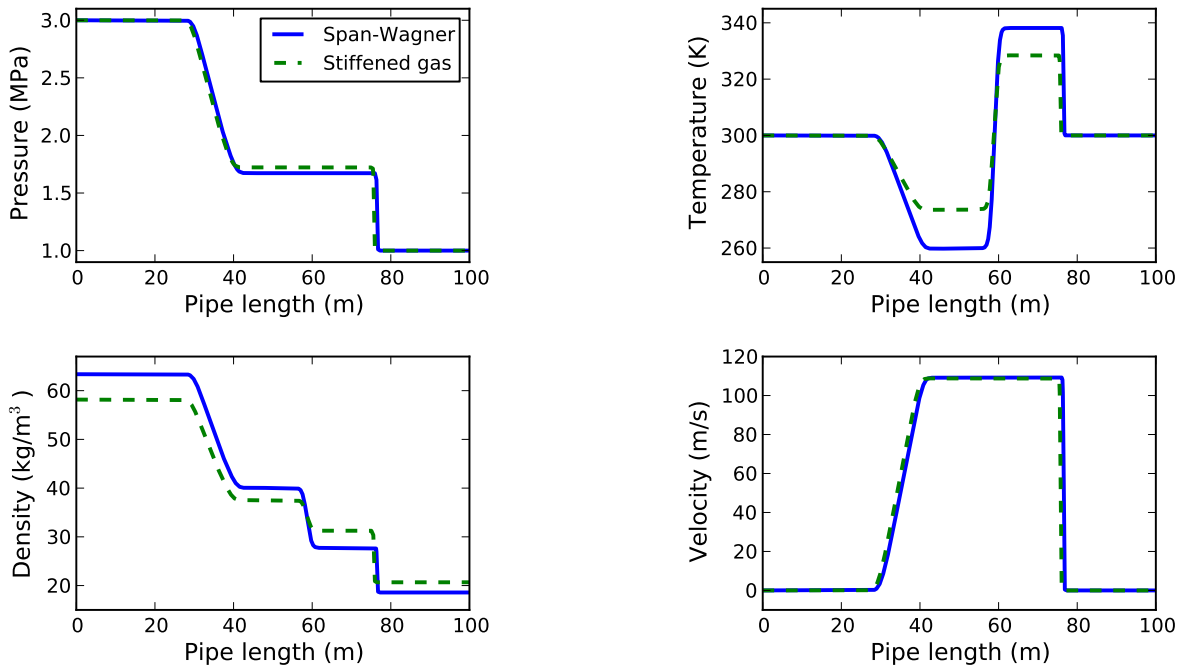


Figure 8: Shock tube test case in the gas phase. Comparison between Span–Wagner and stiffened gas at $t = 0.08$ s.

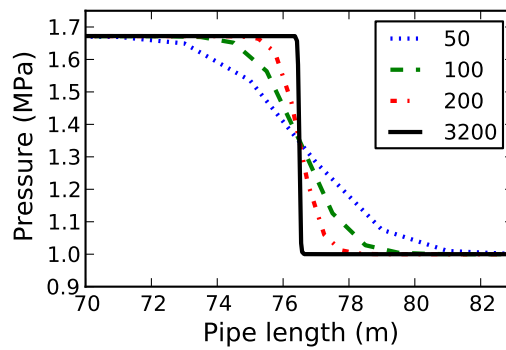


Figure 9: Shock tube test case in the gas phase. Convergence of the pressure with grid refinement.

consider such a depressurization case in which the pipe is initially at 10MPa and $T = 300$ K. At $t = 0$, the pressure at the right-hand boundary is set to 3MPa. A pressure wave will propagate into the pipe and induce a flow towards the right-hand boundary. Due to the reduction in pressure, some of the liquid will evaporate.

The results at $t = 0.2$ s is shown in Figure 10. At the right boundary, the liquid evaporates and the gas fraction eventually reaches a value of 0.48. We also see that the pressure wave splits in two parts. The first part is from the initial pressure down to the vapor pressure, and the second part is in the two-phase region from the vapor pressure down to the outlet pressure. A similar case was considered in Lund et al.³² with the SG EOS. As discussed in that article, the split in the pressure wave is due to a discontinuity in the sound speed when going from pure liquid to two-phase. This is caused by the assumption of equilibrium in pressure, temperature and chemical potential, and is further discussed in Flåtten and Lund.²⁹

Figure 10 shows results for both the SW EOS and the PR EOS. We see that there is an appreciable difference in the results. In particular, the liquid fraction at the end of the domain is very different. Accurate prediction of the liquid fraction can be important, for instance to determine the amount of carbon dioxide released due to a pipeline fracture.

The methods used for solving the ρu problem for the PR EOS are the flash algorithms described in e.g. Michelsen.⁴ The total time of the PR simulation was 20m54s. For the simulation with the SW EOS, the total time was 29m13s. Since the flash algorithms used for the PR EOS are computationally expensive, the PR simulation has similar runtimes as the method presented here, even though the SW EOS is a significantly more complex EOS. We note that the method presented in this work could also be applied to the PR EOS, although that was not attempted here. We also note that the runtimes are obviously dependent on the implementation, so the numbers are only intended as an indication of the computational complexity.

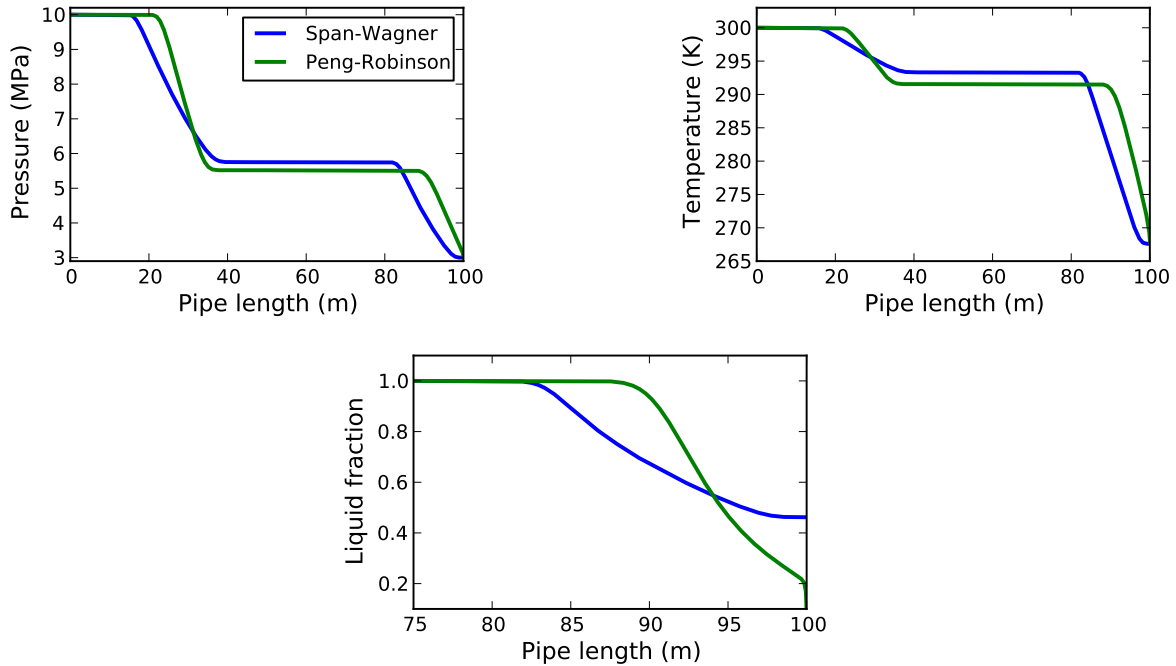


Figure 10: Two-phase depressurization test case. $t = 0.2$ s. Note that the liquid fraction is only plotted for the right end of the domain.

Conclusions

In this work, an algorithm for performing dynamic simulations of systems with pure CO_2 with the Span–Wagner equation of state was presented. The algorithm assumes a density–energy state function and explicitly employs information about the saturation lines which allows for a simpler and more efficient implementation than other approaches. The algorithm was applied to two different problems, a tank model and a fluid–dynamic pipe flow model. The method was shown to be both robust and efficient, and it was demonstrated that the method tackles both single–phase and vapor–liquid problems, and transition between phases.

Further work with respect to the ρu algorithm could be to apply it to other equations of state, either to reference equations for other substances or to simpler equations like the cubic equations of state. It could also be tested for multi–component problems where the composition is constant. A similar approach was for instance used in Arendsen and Versteeg¹³ and Flatby et al.⁶ for tank simulations. For the homogeneous model used in this work for the fluid dynamics, the composition is constant

since the gas and liquid velocities are equal. Hence, the presented method can be used to compute multi-component mixtures together with this fluid dynamic model. To determine which situations this model can be applied to requires experimental validation.

As demonstrated by the final test case, the sound velocity is discontinuous when going from single-phase to two-phase flow for a full equilibrium model. In Flåtten and Lund,²⁹ it is shown that relaxation models can be used to remedy this issue. It would be interesting to see if this concept can be used together with the Span–Wagner equation of state.

Finally, only the presence of gas and liquid was considered in this work. It is well known that dry ice can form for severe depressurizations. The model developed here can be extended with additional equation systems for the solid-vapor and the solid-liquid phases. Together with a model for the thermodynamic properties of the solid phase, this could provide a solid-liquid-vapor model which could be solved with an extension of the presented method.

Acknowledgement

This publication has been produced with support from the BIGCCS Centre, performed under the Norwegian research program Centres for Environment-Friendly Energy Research (FME). The authors acknowledge the following partners for their contributions: Aker Solutions, ConocoPhillips, Det Norske Veritas, Gassco, Hydro, Shell, Statkraft, Statoil, TOTAL, GDF SUEZ and the Research Council of Norway (193816/S60).

We are grateful to our colleagues Øivind Wilhelmsen, Tore Flåtten, Halvor Lund for fruitful discussions, and Morten Hammer for his assistance with some of the simulations.

We thank the anonymous reviewers for carefully reading the manuscript and making several useful remarks.

References

1. Aihara, S.; Misawa, K. Numerical simulation of unstable crack propagation and arrest in CO₂ pipelines. The First International Forum on the Transportation of CO₂ in Pipelines. Newcastle, UK, 2010.
2. Berstad, T.; Dørum, C.; Jakobsen, J. P.; Kragset, S.; Li, H.; Lund, H.; Morin, A.; Munkejord, S. T.; Mølnvik, M. J.; Nordhagen, H. O.; Østby, E. CO₂ pipeline integrity: A new evaluation methodology. *Energy Procedia* **2011**, To appear.
3. Chichilnisky, G.; Heal, G. *Markets for Tradeable CO₂ Emission Quotas Principles and Practice*; OECD Economics Department Working Papers 153, 1995.
4. Michelsen, M. L. State function based flash specifications. *Fluid Phase Equilib.* **1999**, *158-160*, 617 – 626.
5. Gani, R.; Perregaard, J.; Johansen, H. Simulation strategies for design and analysis of complex chemical processes. *Chem. Eng. Res. and Design* **1990**, *68*, 407–417.
6. Flatby, P.; Lundström, P.; Skogestad, S. Rigorous dynamic simulation of distillation columns based on UV-flash. IFAC Symposium ADCHEM'94, Kyoto, Japan. 1994.
7. Eckert, E.; Kubíček, M. Modelling of dynamics for multiple liquid–vapour equilibrium stage. *Chem. Eng. Sci.* **1994**, *49*, 1783 – 1788.
8. Müller, D.; Marquardt, W. Dynamic multiple-phase flash simulation: Global stability analysis versus quick phase determination. *Comput. Chem. Eng.* **1997**, *21*, S817 – S822.
9. Saha, S.; Carroll, J. J. The isoenergetic-isochoric flash. *Fluid Phase Equilib.* **1997**, *138*, 23 – 41.
10. Gonçalves, F.; Castier, M.; Araújo, O. Dynamic simulation of flash drums using rigorous physical property calculations. *Braz. J. Chem. Eng.* **2007**, *24*, 277–286.

11. Castier, M. Solution of the isochoric-isoenergetic flash problem by direct entropy maximization. *Fluid Phase Equilib.* **2009**, *276*, 7 – 17.
12. Castier, M. Dynamic simulation of fluids in vessels via entropy maximization. *J. Ind. Eng. Chem.* **2010**, *16*, 122 – 129.
13. Arendsen, A. R. J.; Versteeg, G. F. Dynamic Thermodynamics with Internal Energy, Volume, and Amount of Moles as States: Application to Liquefied Gas Tank. *Ind. Eng. Chem. Res.* **2009**, *48*, 3167–3176.
14. Span, R.; Wagner, W. A New Equation of State for Carbon Dioxide Covering the Fluid Region from the Triple-Point Temperature to 1100 K at Pressures up to 800 MPa. *J. Phys. Chem. Ref. Data* **1996**, *25*, 1509–1596.
15. Linstrom, P., Mallard, W., Eds. *NIST Chemistry WebBook*; National Institute of Standards and Technology, Gaithersburg MD, 20899, 2011; <http://webbook.nist.gov>, (retrieved February 16, 2011).
16. Huang, F.; Li, M.; Lee, L. L.; Starling, K. E.; Chung, F. T. H. An accurate equation of state for carbon dioxide. *J. Chem. Eng. Japan* **1975**, *18*, 490–496.
17. Kim, Y. Equation of state for carbon dioxide. *J. Mech. Sci. Tech.* **2007**, *21*, 799–803.
18. Lemmon, E. W.; Huber, M. L.; McLinden, M. O. NIST Standard Reference Database 23: Reference Fluid Thermodynamic and Transport Properties-REFPROP, Version 9.0, National Institute of Standards and Technology, Standard Reference Data Program. **2010**, Gaithersburg.
19. Menikoff, R.; Plohr, B. J. The Riemann problem for fluid flow of real materials. *Rev. Mod. Phys.* **1989**, *61*, 75–130.
20. Menikoff, R. *Shock Wave Science and Technology Reference Library, Volume 2 – Solids*; Springer-Verlag: Berlin, 2007; pp 143–188.

21. Peng, D.; Robinson, D. B. A New Two-Constant Equation of State. *Ind. Eng. Chem. Fundamentals* **1976**, *15*, 59–64.
22. Span, R.; Lemmon, E. W.; Jacobsen, R. T.; Wagner, W.; Yokozeki, A. A Reference Equation of State for the Thermodynamic Properties of Nitrogen for Temperatures from 63.151 to 1000 K and Pressures to 2200 MPa. *J. Phys. Chem. Ref. Data* **2000**, *29*, 1361–1433.
23. Michelsen, M. L.; Mollerup, J. *Thermodynamic Models: Fundamentals and Computational Aspects*; Tie-Line Publications, 2007.
24. Haines, E. *Graphics Gems IV: "Point in polygon strategies"*; Academic Press, 1994.
25. Toro, E. F. MUSTA: A multi-stage numerical flux. *Appl. Numer. Math.* **2006**, *56*, 1464–1479.
26. Titarev, V. A.; Toro, E. F. MUSTA schemes for multi-dimensional hyperbolic systems: analysis and improvements. *Int. J. Numer. Meth. Fluids* **2005**, *49*, 117–147.
27. Munkejord, S. T.; Evje, S.; Flåtten, T. The multi-stage centred-scheme approach applied to a drift-flux two-phase flow model. *Int. J. Numer. Meth. Fluids* **2006**, *52*, 679–705.
28. Munkejord, S. T.; Jakobsen, J. P.; Austegard, A.; Mølnvik, M. J. Thermo- and fluid-dynamical modelling of two-phase multi-component carbon dioxide mixtures. *Int. J. Greenh. Gas Cont.* **2010**, *4*, 589–596.
29. Flåtten, T.; Lund, H. Relaxation two-phase flow models and the subcharacteristic condition. *Math. Models Methods Appl. Sci.* **2011**, Accepted.
30. Petzold, L. Description of DASSL: a differential/algebraic system solver. **1982**, SAND-82-8637, Sandia National Laboratories.
31. Zhang, Z.; Wang, G.; Massarotto, P.; Rudolph, V. Optimization of pipeline transport for CO₂ sequestration. *Energy Convers. Manage.* **2006**, *47*, 702 – 715.

32. Lund, H.; Flåtten, T.; Munkejord, S. T. Depressurization of carbon dioxide in pipelines - models and methods. *Energy Procedia* **2011**, To appear.